ACS OMEGA

Open Access

http://pubs.acs.org/journal/acsodf

Article

Numerical Simulation on Erosion and Stress on a Small-Diameter Hydrajet Fracturing Tool

Zhenqiang Xu, Xu Cui, Jing Zhang,* Kaixiang Shen, Xiaoya Wu, and Yiqun Zhang*

Cite This: *ACS Omega* 2024, 9, 11686−11700

Read Online

ACCESS | Metrics & More | Article Recommendations

ABSTRACT: Conventional hydrajet fracturing techniques are often frustrated when they are applied to some specific well types, such as casing-damaged and small-diameter wells. It is of great significance to investigate the erosion and stress on a small-diameter hydrajet fracturing tool during its service and clarify the relevant influencing factors. Based on the solid−liquid two-phase flow theory and erosion model, a numerical simulation was conducted on the erosion and stress on a small-diameter hydrajet fracturing tool by using the computational fluid dynamics approach in order to understand how the inlet flow rate, particle size, and particle mass concentration affect the erosion and stress on the tool. The results show that the erosion on the small-diameter hydrajet fracturing tool is generally a cutting erosion of proppant particles on the tool body. Such erosion occurs on the lower wall of the nozzle, and the erosion at the upper-0° nozzle is higher in rate and smaller in area than that at the lower-180° nozzle. The maximum stress of the small-diameter hydrajet fracturing tool is concentrated on the upper and lower walls of the upper and lower nozzles, especially the lower part inside the upper nozzle. The maximum erosion rate, average erosion rate, and maximum stress on the wall near the nozzle during fracturing increase as the inlet flow rate and particle mass concentration increase and decrease as the proppant particle size increases.

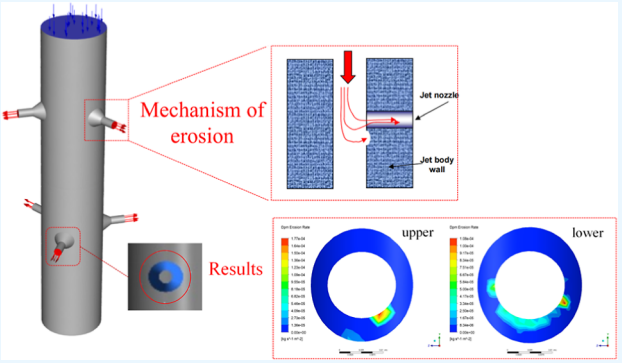

1. INTRODUCTION

In recent years, petroleum exploration and development have gradually turned to unconventional oil and gas reservoirs, of which tight reservoirs are characterized by low porosity, low permeability, low reserve abundance, ultralow water saturation in local areas, high capillary pressure, strong heterogeneity, and multiple thin layers.[1−3] In China, as mature oilfields enter the middle and late stages of development, well production declines rapidly due to reservoir pressure depletion, challenging the oilfield sustainability.[4] Therefore, the efficient, safe, and economical recovery of hydrocarbon resources in low-permeability strata and the stimulation of existing wells are especially important and also significant for the industry sustainability and energy security in the country.[5,6]

Fracturing treatment is a critical technique to enhance the recovery and increase the well production in low-permeability oil reservoirs.[7−9] Typically, hydrajet fracturing, which integrates the advantages of hydrajetting and fracturing,[10,11] has been widely used as a key stimulation method for complex reservoirs and wells, such as low-permeability reservoirs, structurally complex wells, and offshore reservoirs. It is considered as one of the most promising techniques for stimulating unconventional gas reservoirs.[12] For the commercial exploitation of low-permeability shale gas and coalbed gas reservoirs, it can induce hydraulic fractures to expand the single-well sweep area and serve as effective pathways for fluid flow.[13] Natural gas hydrate (NGH) is recognized as a significant and promising clean alternative energy resource in the 21st century.[14−16] In China, the NGH resources are mainly endowed in the argillaceous fine-grained siltstones in the seabed, which have lower gas/water permeability and lower mechanical stability than other deposits.[17] Accordingly, hydrajet fracturing may be a potential contributor to the industrial development of low-permeability argillaceous siltstone NGH reservoirs.[18] Thus, a small-diameter hydrajet fracturing tool is important for the stimulation of unconventional oil and gas reservoirs. As one of its advantages, the tool can complete an efficient fracturing operation in confined space while minimizing the damage to the underground reservoir.

As a lot of oilfields enter the middle and late stages of development, more and more casing-deformed wells and slim holes appear, and the small-diameter hydrajet fracturing process

Received: November 15, 2023
Revised: February 9, 2024
Accepted: February 13, 2024
Published: March 1, 2024

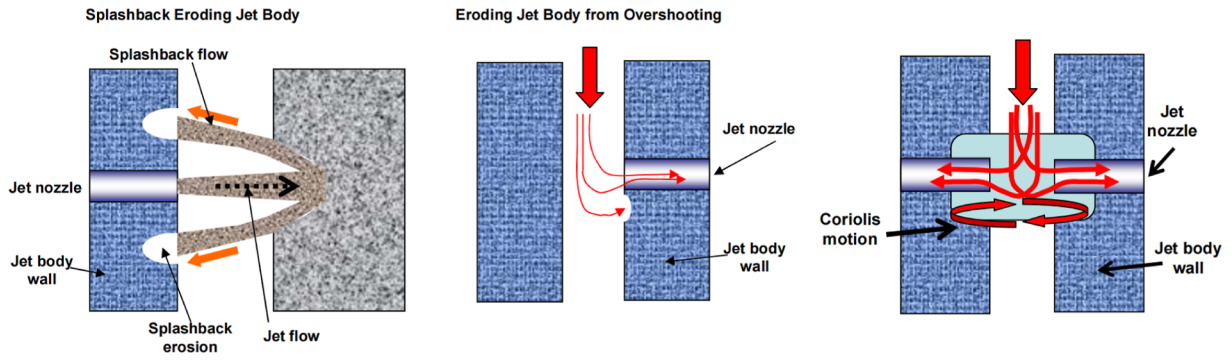

Figure 1. Mechanism of erosion on the hydrajet fracturing tool.

is increasingly demanded.[19−21] In China, rapid progress in shale gas exploration and development is associated with a frequent occurrence of casing deformation in horizontal wells, which directly affects the efficiency and profitability of shale gas development. Casing deformation reduces the inner diameter of casing, so that the conventional tubing-based fracturing operation is hindered, resulting in more frequent casing damages in wells, some of which are even ultimately shut down.[22,23] In this regard, small-diameter hydrajet fracturing has become more and more necessary. The small-diameter hydrajet fracturing tool is mainly employed to extract the remaining oil and gas resources in reservoirs for revitalizing the productivity of existing wells, improving the recovery, extending the well life, and mitigating environmental impacts. It provides a sustainable and economical solution for the petroleum industry.

Hydrajet fracturing process combines hydrajet perforation, fracturing, and hydraulic isolation, which are completed in one trip of string, enabling a higher operation efficiency and a shorter operation period. In hydrajet fracturing, with a high flow rate and a high proppant-to-liquid ratio, the presence of substantial high-velocity proppant particles may erode seriously the fracturing tool, leading to a considerable reduction in the service life of high-pressure manifolds.[24]

For the small-diameter hydrajet fracturing tool, previous studies focused on the flow field and parameters of the erosion model. However, erosion on the small-diameter fracturing tools has rarely been reported. According to the computational fluid dynamics (CFD) theory, Clem et al. (2006)[25] investigated the flow behaviors in the fracturing string at high flow rates, analyzed the relationships between the flow velocity, stream line and proppant concentration the scouring, and presented an optimized structure of the string. M Sheng et al. (2019)[26] proposed a 3D CFD-based erosion model by considering high-velocity waterjet impact, proppant shear erosion, and specific inner structure of hydrajet tool body. The discrete phase approach was used to track the proppant transport and its concentration distribution. Field observation provides strong evidence of erosion patterns and mechanisms obtained from CFD simulation. Li and Hamid et al. (2005)[27] used a CFD model to determine the fluid flow regime near the sand jet in a horizontal well. Based on the CFD theory, Li et al. (2009)[28] built a particle erosion model, which considers the collision between particles and was used to determine the motion characteristics and erosion patterns of solid particles in the solid−liquid two-phase flow within the choke during hydrajet fracturing operation, indicating that the distribution of solid particles is irregular, with a concentration of solid particles observed in the region from the inlet to the outlet of the choke, and an exponential relationship exists between the material erosion rate and the fluid flow rate. Xu et al. (2022)[29] based on CFD, discrete phase model (DPM), and optimal design theory, this paper uses ANSYS workbench software to numerically simulate the erosion of 2.375″ coiled tubing wound on the drum by fracturing fluid. The simulation result shows that the coiled tubing erosion rate is most affected by the fracturing fluid injection velocity. Gravel mass flow rate has less effect. Gravel diameter has the least effect. Surjaatmadja et al.[30,31] investigated the mechanism of internal and/or external erosion during conventional hydrajet perforating. They identified two distinct mechanisms of erosion on the body and nozzle of the jetting tool. To be specific, the tool body can encounter a wear induced by splashback erosion, overshooting, or Coriolis erosion, as illustrated in Figure 1; the nozzle primarily suffers from an erosion of sliding particles, following the mechanism of microcutting, microdeformation, or fatigue. Cui et al.[32] extracted the parameters of single-cluster hydrajet fracturing in field application and numerically simulated the anti-erosion performance of the hydrajet body material (35CrMo steel). Their findings indicate that the presence of abrasive particles results in erosion on 35CrMo steel, which is induced by microcutting when the impact angle is small and by impact forging when the impact angle is large, and that the erosion rate of the specimen peaks when the impact angle is 45°.

In the conventional hydrajet fracturing process, which exhibits high flow rate and high proppant-to-liquid ratio, the presence of substantial proppant particles flowing at a high rate erodes seriously the fracturing tool.[33] In contrast, during small-diameter hydrajet fracturing, when the fracturing fluid flows at a higher rate, the high-velocity proppant particles carried in the fluid may have more serious erosion on the tool, which will lead to tool failure, significantly impeding the fracturing operation. Thus, it is necessary to investigate and predict the erosion and stress on a small-diameter hydrajet fracturing tool and facilitate an optimization of the tool structure for ensuring the success of fracturing operations and the service life of the tool.

Here, by using the CFD approach, the erosion and stress on small-diameter hydrajet fracturing tool are numerically simulated to determine the flow field, erosion distribution, and stress variation of the hydrajet tool under various operational parameters (e.g., inlet flow rate, proppant particle size, and proppant particle mass concentration). The findings provide valuable references for understanding the erosion on a small-diameter hydrajet fracturing tool for the purpose of structural optimization.

https://doi.org/10.1021/acsomega.3c09102
ACS Omega 2024, 9, 11686−11700

2. COMPUTATIONAL MODELING

Trace of the particle motion path is crucial to the determination of erosion on the tool wall. The particle motion near the tool wall primarily involves impact and rebound. Hence, a discrete model is preferable for calculating the rate of erosion on the internal wall of the tool (hereinafter referred to as internal erosion). In the discrete model, solid particles are considered in discrete status, while the liquid phase is treated as a continuous medium. To analyze the distribution of stress on the tool body, a solid−liquid two-phase flow model is used. This model treats the liquid and solid phases as two continuous fluids that are interactive and independent.

2.1. Liquid Phase Control Equation. Continuity equation is given as follows

$$\frac{\partial(\alpha_f\rho)}{\partial t} + \frac{\partial(\alpha_f\rho u_j)}{\partial x_j} = 0 \tag{1}$$

where ∂_f is the liquid phase volume fraction; ρ is the liquid phase density, kg/m^3; u is the liquid phase velocity, m/s; and t is the time, s.

Momentum equation is given as follows

$$\frac{\partial(\alpha_f\rho u_i)}{\partial t} + \frac{\partial(\alpha_f\rho u_i u_j)}{\partial x_j} = -\alpha_f\frac{\partial p}{\partial x_i} + \alpha_f\frac{\partial \tau_{ij}}{\partial x_j} + \alpha_f\rho g_i + F_i \tag{2}$$

where p is the hydrostatic pressure acting on the fluid element, Pa; τ is the liquid phase stress tensor, determined by $\tau_{ij} = \left[\mu\left(\frac{\partial u_i}{\partial x_j} + \frac{\partial u_j}{\partial x_x}\right)\right] - \frac{2}{3}\mu\frac{\partial u_l}{\partial x_l}\delta_{ij}$; and F is the interphase interaction force per unit volume.

2.2. Solid Phase Control Equation. The motion paths of discrete particles are determined by integrating the momentum equation for particles in a Lagrangian coordinate system. The momentum equation for particles can be derived from the Newton's second law, as shown in eq 3[34]

$$\frac{d\vec{u}_p}{dt} = F_D(\vec{u} - \vec{u}_p) + \frac{g(\rho_p - \rho)}{\rho_p} + \vec{F} \tag{3}$$

where $\vec{u}$ is the fluid phase velocity; $\vec{u}_p$ is the particle velocity; ρ is the fluid density; and ρ_p is the particle density.

In addition, $F_D = (\vec{u} - \vec{u}_p)$ is the particle drag force per unit mass, and

$$F_D = \frac{18\mu}{\rho_p d_p^2}\frac{C_D\mathrm{Re}}{24} \tag{4}$$

where μ is the dynamic viscosity of the fluid; Re is the particle Reynold's number, defined as

$$\mathrm{Re} = \frac{\rho d_p|\vec{u}_p - \vec{u}|}{\mu} \tag{5}$$

and C_D is the drag coefficient, determined by $C_D = \alpha_1 + \frac{\alpha_2}{\mathrm{Re}} + \frac{\alpha_3}{\mathrm{Re}^2}$.

2.3. Turbulent Flow Model. The calculation of Reynold's number suggests that the target fluid in this study follows a turbulent flow pattern. Thus, a turbulent flow model is required. Transport equations for the turbulent kinetic energy (k) and turbulent dissipation rate (ε) in the realizable k-ε model are expressed as[35]

$$\frac{\partial}{\partial t}(\rho k) + \frac{\partial}{\partial x_j}(\rho k u_j) = \frac{\partial}{\partial x_j}\left[\left(\mu + \frac{\mu_t}{\sigma k}\right)\frac{\partial k}{\partial x_j}\right] + G_k + G_b - \rho\varepsilon - Y_M + S_k \tag{6}$$

$$\frac{\partial}{\partial t}(\rho\varepsilon) + \frac{\partial}{\partial x_j}(\rho\varepsilon u_j) = \frac{\partial}{\partial x_j}\left[\left(\mu + \frac{\mu_t}{\sigma\varepsilon}\right)\frac{\partial \varepsilon}{\partial x_j}\right] + \rho C_1 S\varepsilon - \rho C_2\frac{\varepsilon^2}{k + \sqrt{\nu\varepsilon}} + C_{1\varepsilon}\frac{\varepsilon}{k}C_{3\varepsilon}G_b + S_\varepsilon \tag{7}$$

where G_b is the turbulent kinetic energy due to buoyancy; G_k is the turbulent kinetic energy due to the mean velocity gradient; Y_M is the contribution of the pulsating expansion of the compressible turbulent flow to the total dissipation rate; C_{1s} and C_{2s} are empirical constants; σ_k and σ_s are the Prandtl numbers corresponding to the k and ϵ equations; and S_k and S_s are the self-defined turbulent kinetic energy and turbulence dissipation source terms. Defaults in Fluent include $C_{1s} = 1.44$, $C_{2s} = 1.9$, $\sigma_k = 1.0$, and $\sigma_s = 1.2$.

$$C_1 = \max\left[0.43, \frac{\eta}{\eta + 5}\right], \quad \eta = S\frac{k}{\varepsilon}, \quad S = \sqrt{2S_{ij}S_{ij}}$$

In the realizable k-ε model, the eddy viscosity is calculated by

$$\mu_t = \rho C_\mu\frac{k^2}{\varepsilon} \tag{8}$$

where

$$C_\mu = \frac{1}{A_0 + A_s\frac{kU^*}{\varepsilon}}, \quad U'' \equiv \sqrt{S_{ij}S_{ij} + \tilde{\Omega}_{jj}\tilde{\Omega}_{ij}}$$

$$\tilde{\Omega}_{jj} = \Omega_{jj} - 2\varepsilon_{ij}w_k, \quad \Omega_{jj} = \bar{\Omega}_{ij} - \varepsilon_{ijk}w_k$$

2.4. Solid−Liquid Two-Phase Flow Model. As described above, the solid−liquid two-phase flow model treats the liquid and solid phases as two continuous fluids that are interactive and independent. This model is constructed using two sets of equations that separately describe the motion of each phase and couple them through interphase interaction forces. In this model, both solid and liquid velocities are regarded as local averages and random components. Eventually, the continuity equation and momentum equation for the two-phase flow model can be derived as follows:[36−38]

Liquid phase

$$\frac{\partial\rho^f}{\partial t} + \nabla(\rho^f u_f) = 0(\text{no phase change}) \tag{9}$$

$$\rho^f\left[\frac{\partial u_f}{\partial t} + (u_f\nabla)u_f\right] = \rho^f g - F + \nabla((1 - \alpha_p)T_f) \tag{10}$$

Solid phase

$$\frac{\partial\rho^p}{\partial t} + \nabla(\rho^p u_p) = 0(\text{no phase change}) \tag{11}$$

$$\rho^p\left[\frac{\partial u_p}{\partial t} + (u_p\nabla)u_p\right] = \rho^p g - F + \nabla((1 - \alpha_p)T_p) \tag{12}$$

where $\rho^f = \rho_f(1 - \alpha_p)$ and $\rho^p = \rho_p\alpha_p$, which denote the local densities of the liquid and solid phases, respectively; F is the

https://doi.org/10.1021/acsomega.3c09102
ACS Omega 2024, 9, 11686−11700

interphase interaction force per unit volume; and T_p and T_f are the stress tensors for the solid and fluid phases, respectively.

2.5. Erosion Model. *2.5.1. Definition of the Erosion Rate.* The solid−liquid two-phase flow model for erosion simulation incorporates parameters including impact angle function, wall function, fluid velocity, viscosity, particle size, and particle mass flow rate. The erosion rate, expressed in unit of kg/(m^2·s), is defined as the mass of wall material eroded per unit area per unit time.

In Fluent, the erosion rate is defined as

$$R_{\text{erosion}} = \sum_{p=1}^{N_{\text{pesside}}} \frac{\dot{m}_p C(d_p) f(\alpha) v_p^{b(v_p)}}{A_{\text{wall}}} \tag{13}$$

where $\dot{m}_p$ is the mass flux of the pth particle; $C(d_p)$ is the particle size function, usually set as 1.8×10^{-9}; α is the impact angle between the particle path and the wall; $f(\alpha)$ is the impact angle function; v_p is the particle impact velocity; $b(v_p)$ is the particle impact velocity function, commonly set as 2.6 according to previous research and field data; A_{wall} is the wall area; N_{particle} is the number of particles; C, f, and b are essential boundary conditions for the wall and determined empirically depending on particles and materials; and the product $C(d_p)f(\alpha)v_p^{b(v_p)}$ represents the erosion rate, which is defined as the mass of wall material eroded per unit mass of particles impacting the wall.

2.5.2. Impact Angle Function. Materials display varying erosion patterns at different impact angles. Typically, plastic materials exhibit the maximum erosion rate at the impact angle of 15−30°, while brittle materials exhibit the maximum erosion rate at the impact angle of 90°.[39]

In this study, the tool body is made of a plastic material, grade 45 steel, with low erosion resistance, and the nozzle is made of a brittle material, hard alloy, with high erosion resistance. Thus, the inlet region of the tool body is specifically investigated.

2.5.3. Particle Rebound Coefficient. When a solid particle collides with the wall and rebounds, a part of its energy is lost or transferred, which is manifested in the change of particle velocity before and after the collision, as illustrated in Figure 2. Usually,

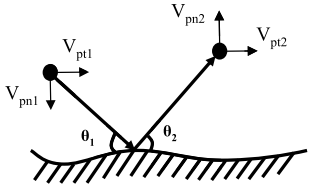

Figure 2. Particle rebound on the wall.

the ratio of the postcollision velocity component to the precollision velocity component is defined as the rebound coefficient, which is used to characterize the energy loss when particles collide with the wall. This coefficient is categorized into the normal rebound coefficient e_n and the tangential rebound coefficient e_t, expressed as

$$e_n = \frac{V_{pn2}}{V_{pn1}} \tag{14}$$

$$e_t = \frac{V_{pt2}}{V_{pt1}} \tag{15}$$

where V_{pn} and V_{pt} are the velocity components of particles in the normal and tangential directions, respectively; subscript 1 denotes the state of particles before collision; and subscript 2 denotes the state of particles after collision.

Many researchers, such as Forder et al.[40] and Grant and Tabakoff,[41] have devised several rebound coefficient models through experiments under different particle characteristics and collision conditions. In this study, the Grant and Tabakoff rebound coefficient model is selected, as follows

$$e_n = 0.993 - 1.76\alpha + 1.56\alpha^2 - 0.49\alpha^3 \tag{16}$$

$$e_t = 0.998 - 1.66\alpha + 2.11\alpha^2 - 0.67\alpha^3 \tag{17}$$

where α is the particle impact angle, rad.

The rebound coefficient model is combined with the erosion model to trace the particle path and compute the erosion rate.

3. GEOMETRIC MODEL AND CONDITION SETTING

3.1. Geometric Modeling. The geometric model of hydrajet for small-diameter multicluster fracturing was constructed using SolidWorks, as shown in Figure 3. The hydrajet

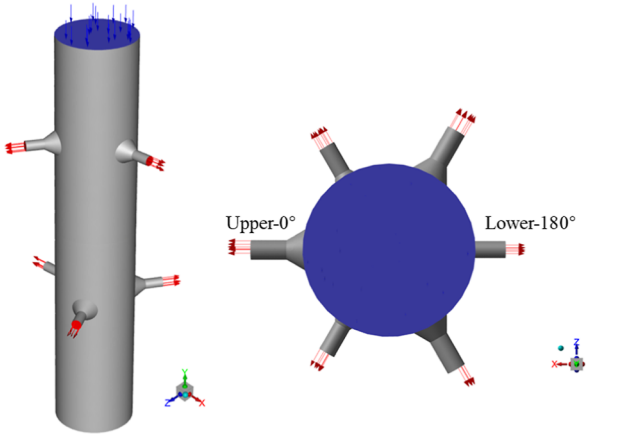

Figure 3. Physical model of the hydrajet for small-diameter multicluster fracturing.

body has an inner diameter of 48 mm, an outer diameter of 84 mm, and a length of 250 mm. The nozzles are segmented into upper and lower clusters spaced 100 mm. Each cluster consists of three nozzles arranged in a 120° helical pattern. The nozzle is conical internally, with a length of 18 mm, a convergence angle of 60°, and a diameter of 6 mm. Two nozzles, named as the upper-0° nozzle and the lower-180° nozzle depending on their positions in the layers and phases, are selected for analysis.

The hydrajet body is made of grade 45 steel with a density of 7800 kg/m^3, and the nozzle is made of hard alloy with a density of 15,000 kg/m^3. Based on field data, the initial values of parameters are set as follows: fracturing fluid density of 1050 kg/m^3, fracturing fluid viscosity of 0.003 Pa·s, and particle density of 2650 kg/m^3. The gravity of the fluid and the particles is set with a gravitational acceleration of −9.81bn m/s^2 on the y-axis. The erosion on the tool was tested at varying particle sizes (0.4 0.5, 0.6, 0.8, and 1.0 mm), fracturing fluid flow rates (1.4, 1.6, 1.8, 2.0, and 2.2 m^3/min), and particle mass concentrations (80, 100, 120, 140, and 160 kg/m^3).

3.2. Meshing. The model of the hydrajet is divided into tetrahedral meshes. Field operations demonstrate that tool failure generally occurs because the tool body is preferentially eroded at the junction of the tool body and the nozzle due to their different materials. Here, the junction region is divided into

https://doi.org/10.1021/acsomega.3c09102
ACS Omega 2024, 9, 11686−11700

more dense meshes. The model is finally divided into 569,847 meshes, with 113,072 nodes (Figure 4).

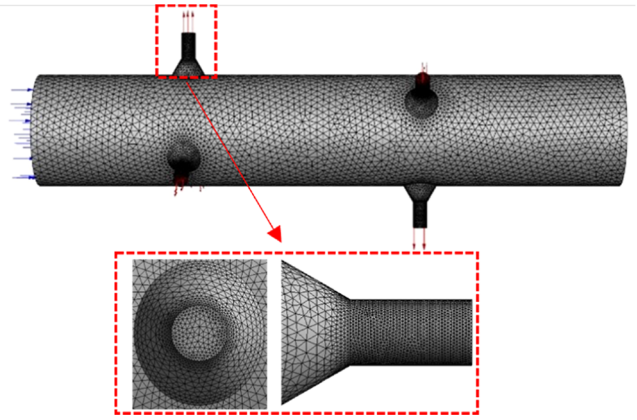

Figure 4. Meshing and enlarged view of the refined grid of nozzle locations.

3.3. Grid Independence Analysis and Model Validation. To eliminate the effect of grid number, grid independence analysis of the simulation results was conducted. In order to analyze the grid sensitivity in this simulation, the grid number was adjusted and designed to be 202,819, 326,023, 569,847, and 851,929; the calculation was carried out under the same boundary conditions; and the axial velocity of the center section was selected as the comparison object, and the results are shown in Figure 5. In order to ensure the accuracy of the calculation and the time cost of the calculation, the final number of grids was chosen to be 569,847.

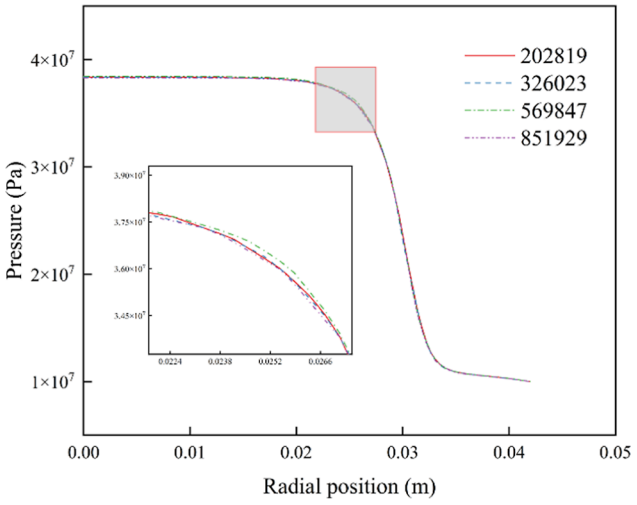

Figure 5. Pressure curves for different number of meshes.

3.4. Setting of Boundary Conditions and Other Parameters. The velocity inlet boundary condition is used and is determined from the injection flow rate on site. The nozzle outlet serves as the model's outlet boundary and utilizes the pressure outlet boundary condition, with the outlet pressure set to 10 MPa. The tool body and nozzle surfaces act as the model's wall boundary, and nonslip solid-wall conditions are applied in a rebound case; that is, a particle rebounds upon collision with the wall and then re-enters the computational domain. The impact angle function is assigned for both the tool body and nozzle walls (Table 1). The particle rebound coefficient is given in Table 2, and the particle size function and velocity index function are listed in Table 3. Particles are injected by surface jetting, in a direction perpendicular to the inlet end face, and the particle random wandering model is activated.

Table 1. Erosion Angle Function

point	impact angle α (deg)	impact angle function $f(\alpha)$
1	0	0
2	20	0.8
3	30	1.0
4	45	0.5
5	90	0.4

Table 2. Particle Rebound Coefficient

	α^0	α^1	α^2	α^3
normal	0.993	−0.0307	4.75×10^{-4}	-2.61×10^{-6}
tangential	0.998	−0.0290	6.43×10^{-4}	-3.56×10^{-6}

Table 3. Particle Size Function and Velocity Index

C(dp)	n
$1.8 \times 10-^{9}$	2.6

In this study, the adopted realizable k-ε model can simulate the internal flow field of the fracturing fluid, and the DPM is employed to simulate the particle motion and examine the erosion rate in the erosion module. The above two models are coupled to investigate the erosion on the small-diameter hydrajet fracturing tool. Moreover, the Euler solid−liquid two-phase model is applied to investigate the stress on the small-diameter hydrajet fracturing tool. During the solution, the pressure−velocity coupling follows the SIMPLE algorithm, and a second-order upwind scheme is used for the discretization of momentum, turbulent kinetic energy, and turbulent dissipation rate.

3.5. Model Validation. The hydrajet used in fracturing of Well A in the Erlian Basin, China, was analyzed for the erosion on the inner wall by means of the 3D morphology scanning technology, in order to validate the proposed model.

In well A, fracturing was conducted by injection through tubing and casing simultaneously at a flow rate of 2.2 m^3/min, and the tool was tripped out after fracturing for 2 h. Figure 6 reveals the erosion on the inner walls of the hydrajet.[42] The same operating conditions are numerically simulated (Figure 7), and the 3D morphology of the dissected hydrajet is scanned using an Artec-spider 3D scanner (Figure 8). It can be seen that the numerical simulation results are consistent with the actual erosion patterns shown in Figure 5. Specifically, the lower inlet regions of both the lower and upper nozzles are eroded most severely, which verifies the accuracy of the proposed model.

4. DISCUSSION

4.1. Flow Field. The selected proppant particles correspond to an average diameter of 0.4 mm, a flow rate of 2.1 m^3/min, and a mass flow rate of 1 kg/s. The pressure and flow velocity distributions in the flow field of the tool are obtained through numerical simulation, and the flow fields of the upper-0° and

https://doi.org/10.1021/acsomega.3c09102
ACS Omega 2024, 9, 11686−11700

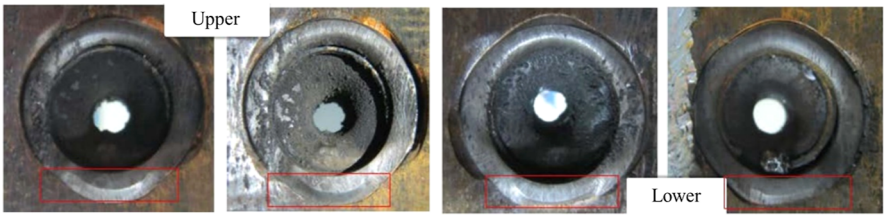

Figure 6. Erosion on the inner wall of the hydrajet.

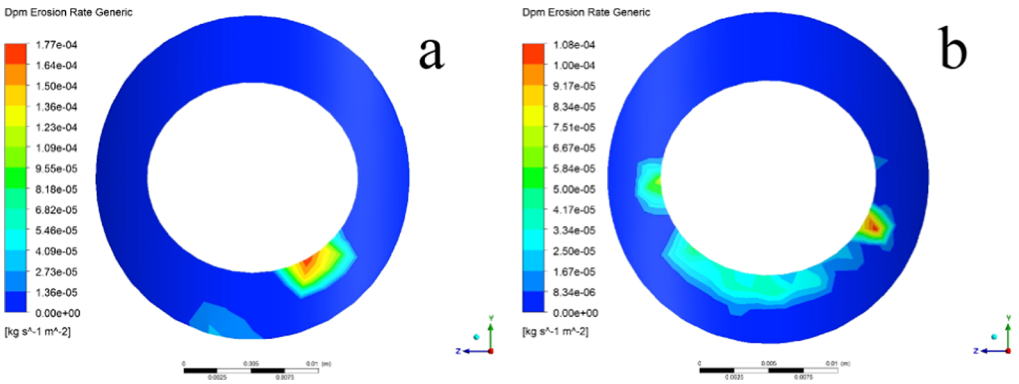

Figure 7. Erosion rate contours of the inlet region under the experimental conditions: (a) upper nozzle and (b) lower nozzle.

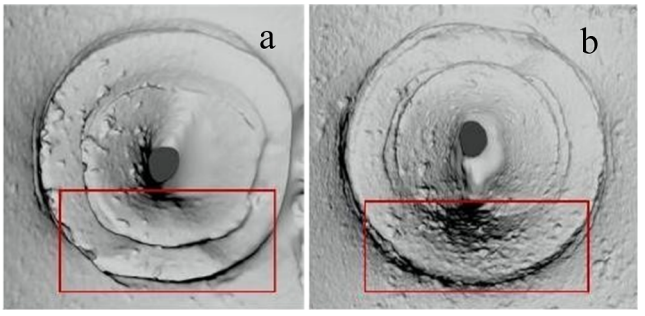

Figure 8. 3D scan image of the inlet region: (a) upper nozzle and (b) lower nozzle.

lower-180° nozzles are compared to infer the erosion differences.

4.1.1. Pressure Distribution. Figure 9 shows the nephogram of static pressure on the axial cross-section of the tool. The part from the outlets of the upper-0° nozzle and lower-180° nozzle to the axial center of the tool is selected for analysis to determine the change in the static pressure on the axis of the nozzles with the radial position. As shown in Figure 10, the static pressure inside the nozzle starts to decrease, and the pressure distributions of the upper-0° nozzle and the lower-180° nozzle are similar, with the pressure decreasing from the upper part of the nozzle−body junction.

4.1.2. Flow Velocity Distribution. Figure 11 shows the nephogram of fluid velocity on the axial cross-section of the tool. The part from the outlets of the upper-0° nozzle and lower-180° nozzle to the axial center of the tool is selected for analysis to determine the change in the flow velocity on the axis of the nozzles with the radial position. As shown in Figure 12, the flow velocity remains constant basically within the tool body. As the nozzle diameter reduces, the flow velocity increases sharply up to 233 m/s, which is much higher than the flow velocity required for rock breaking (180 m/s).[43] The fluid velocity in the upper-0° nozzle is 8 m/s higher than that in the lower-180° nozzle.

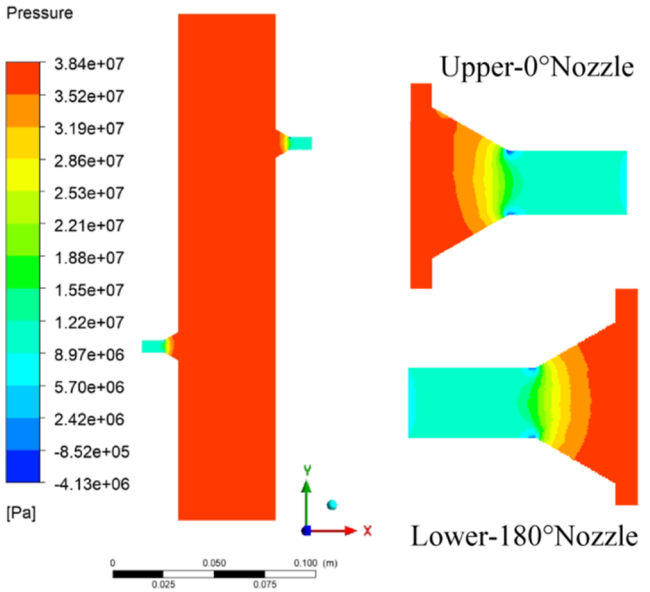

Figure 9. Static pressure on the axial cross-section of the tool and enlarged view of the nozzle.

Furthermore, the flow velocity is different above and below the inlet of the upper-0° nozzle but identical above and below the inlet of the lower-180° nozzle. This observation suggests that the upper-0° nozzle is more seriously impacted by the fracturing fluid at the inlet, while the lower-180° nozzle is more extensively impacted by the fracturing fluid.

4.1.3. Proppant Particle Volume Distribution. Figure 13 shows the nephogram of propant distribution on the axial cross-section of the tool. It can be seen that the proppant particles are concentrated on the lower wall of the nozzle, the maximum particle volume fraction is found on the lower wall of the upper nozzle, the volume distribution of proppant particles is more extensive in the lower nozzle, and there are basically no proppant particles settled at the bottom of the tool.

https://doi.org/10.1021/acsomega.3c09102
ACS Omega 2024, 9, 11686−11700

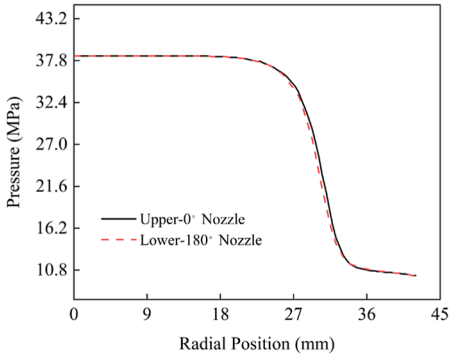

Figure 10. Static pressure vs radial position of the nozzle.

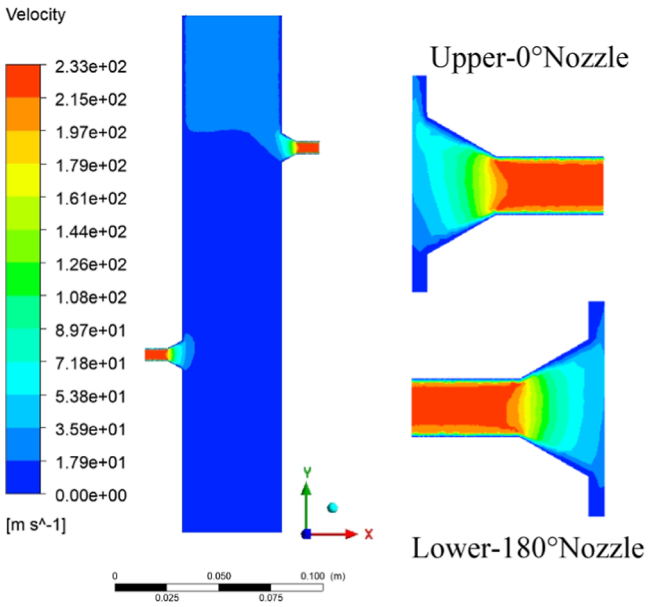

Figure 11. Flow velocity on the axial cross-section and enlarged view of the nozzle.

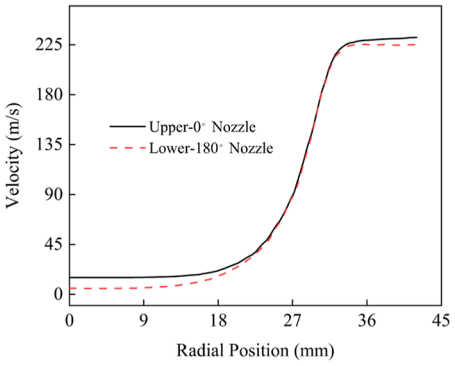

Figure 12. Flow velocity vs radial position of the nozzle.

4.2. Factors Affecting the Erosion and Stress on the Tool. *4.2.1. Flow Rate.* Given the fracturing fluid with a viscosity of 0.003 Pa·s, a mass flow rate of 1 kg/s, a particle size of 0.4 mm, and a particle injection velocity consistent with the fluid flow velocity, a numerical simulation is conducted at the flow rates of 1.4 m^3/min, 1.6, 1.8, 2.0, and 2.2 m^3/min, respectively. Then, the erosions in the inlet regions of the upper-0° and lower-180° nozzles at different flow rates are determined, as shown in Figure 14. It can be seen that the erosion positions in the inlet regions remain roughly consistent at different flow rates. The maximum erosion rates in the upper nozzle are concentrated in the lower right corner of the inlet region. Moreover, the lower nozzle exhibits a larger erosion area, with the maximum erosion rates concentrated in the lower part of the inlet region.

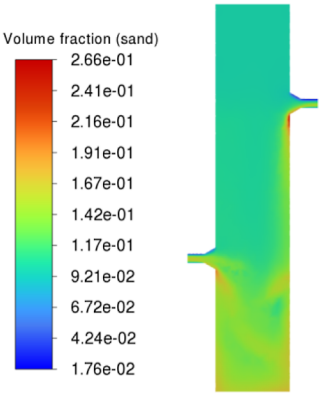

Figure 13. Proppant particle volume fraction.

Figure 15 shows the maximum erosion rate at different flow rates. As the flow rate increases, the maximum erosion rate in the inlet region of the upper-0° nozzle or of the lower-180° nozzle tends to increase exponentially. Exponential fitting is performed on the data, yielding an exponent of 1.8552 for the upper nozzle and 2.357 for the lower nozzle. At each flow rate, the maximum erosion rate in the inlet region of the upper-0° nozzle is higher than that in the inlet region of the lower-180° nozzle.

Figure 16 shows the average erosion rates at different flow rates. Generally, as the flow rate increases, the average erosion rate increases exponentially. The direct proportionality between flow rate and fluid velocity indicates that the particle velocity has a significant impact on the erosion rate. At each flow rate, the average erosion rate in the inlet region of the lower-180° nozzle is higher than that in the inlet region of the upper-0° nozzle. This implies a more serious erosion in the inlet region of the lower nozzle.

Figure 17 shows the stress distribution of the tool at different flow rates derived from ANSYS analysis. Notably, the maximum stress in the tool is concentrated on the upper and lower walls of the upper and lower nozzles, especially the lower part inside the upper nozzle.

Figure 18 illustrates the variation of the maximum stress with the flow rate. A linear relationship is found, that is, the maximum stress increases with the increasing flow rate. Coupling with the propant distribution shown in Figure 12, it can be deduced that the lower parts of the upper and lower nozzles are subjected to particle impact. As the flow rate increases, the stress on the tool increases gradually, and the erosion rate also increases.

4.2.2. Particle Size. Given the fracturing fluid with a viscosity of 0.003 Pa·s, a flow rate of 2.1 m^3/min, a mass flow rate of 1 kg/s, and a particle injection velocity consistent with the fluid flow velocity, a numerical simulation is conducted at the particle sizes of 0.4, 0.5, 0.6, 0.8, and 1.0 mm, respectively. Then, the erosions in the inlet regions of the upper-0° and lower-180° nozzles at different particle sizes are determined, as shown in Figure 19. It can be seen that the erosion positions in the inlet regions remain roughly consistent at different particle sizes. The maximum erosion rates in the upper nozzle are concentrated at the lower right corner of the inlet region. Moreover, the lower nozzle exhibits a larger erosion area, with the maximum erosion rates concentrated in the lower part of the inlet region. The erosion of

https://doi.org/10.1021/acsomega.3c09102
ACS Omega 2024, 9, 11686−11700

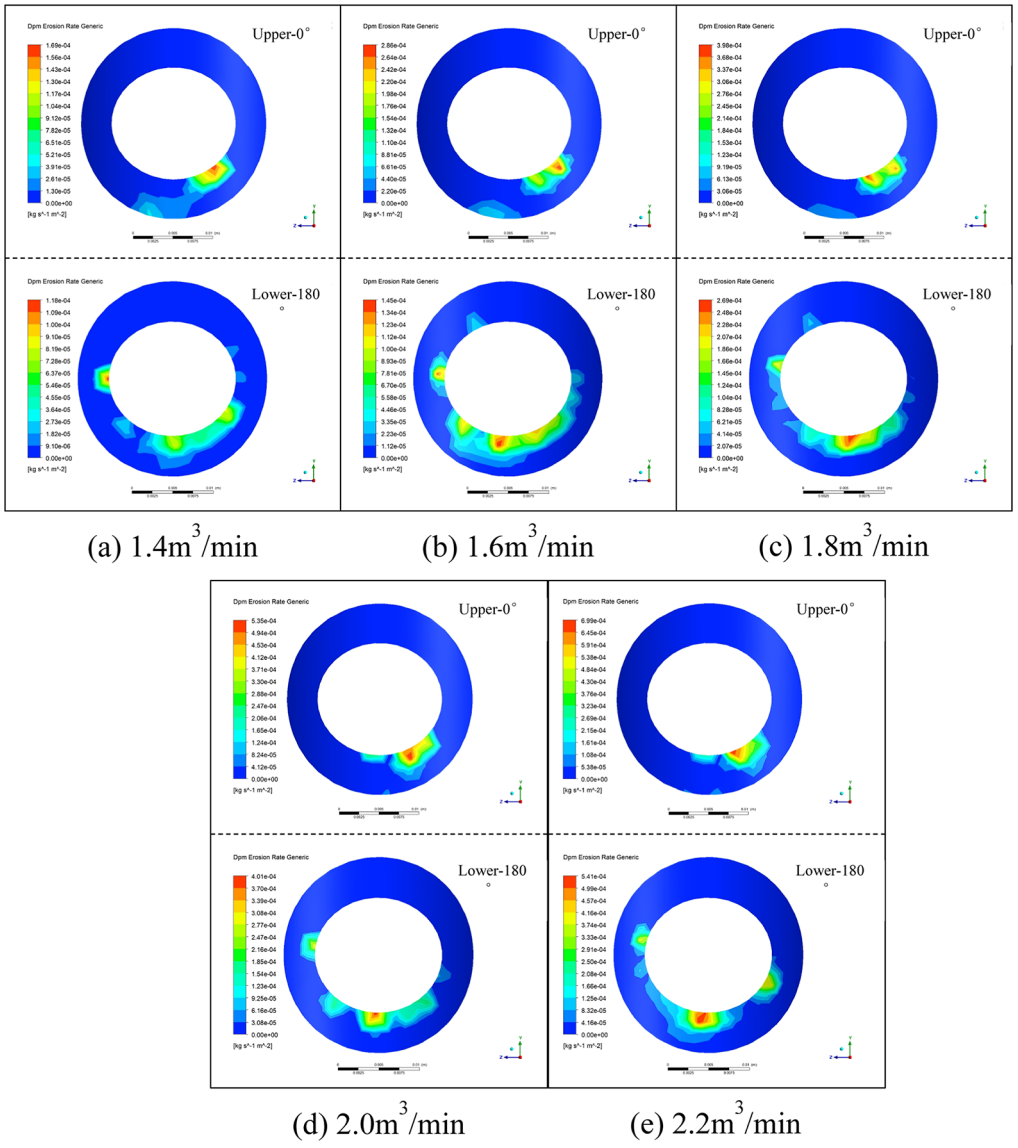

Figure 14. Erosion rate in the inlet regions of the upper-0° and lower-180° nozzles at different flow rates.

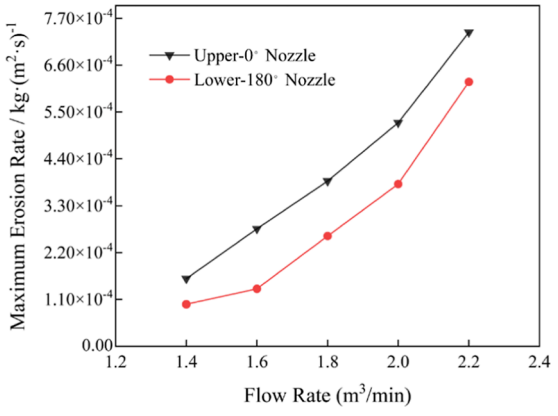

Figure 15. Maximum erosion rate vs flow rate in the inlet regions of the upper-0° and lower-180° nozzles.

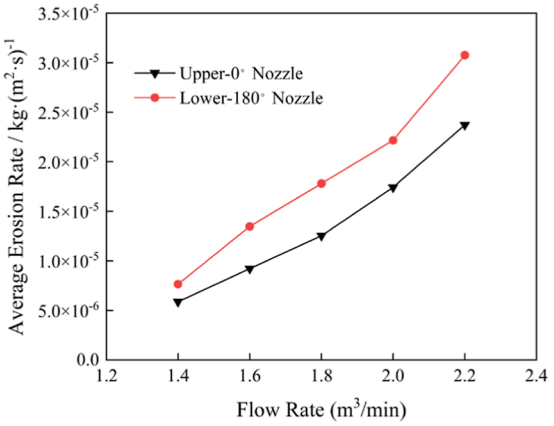

Figure 16. Average erosion rate vs flow rate in the inlet regions of the upper-0° and lower-180° nozzles.

particles is more noticeable when the particle size is less than 0.6 mm.

Figure 20 shows the maximum erosion rates at different particle sizes. A negative correlation is seen, that is, with the increase of particle size, the maximum erosion rate decreases gradually. Moreover, the maximum erosion positions occur in the inlet region of the upper-0° nozzle. A turn appears in the

https://doi.org/10.1021/acsomega.3c09102
ACS Omega 2024, 9, 11686−11700

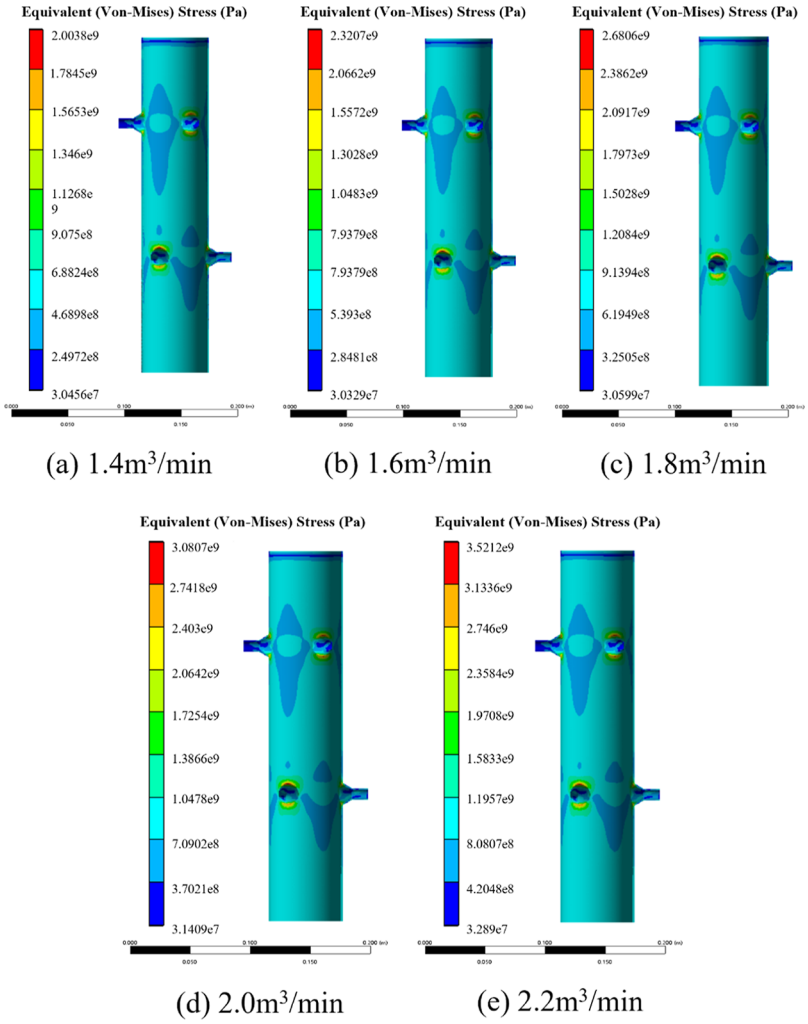

Figure 17. Stress distribution at different flow rates.

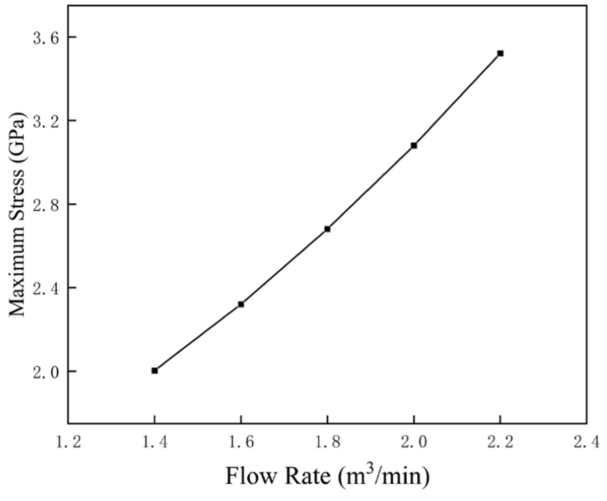

Figure 18. Maximum stress vs flow rate.

decrease of the maximum erosion rate at the particle size of 0.6 mm: the maximum erosion rate decreases faster when the particle size is less than 0.6 mm but slower when the particle size is greater than 0.6 mm. At each particle size, the maximum erosion rate in the inlet region of the upper-0° nozzle is higher than that in the inlet region of the lower-180° nozzle.

Figure 21 shows the average erosion rate at different particle sizes. With the increase of particle size, the average erosion rate in the inlet region of the nozzle decreases. When the mass flow rate and density of the particles are constant, with the increase of particle size, the number of particles reduces and the frequency of impact on the wall declines; overall, the average erosion rate decreases gradually. At each particle size, the average erosion rate in the inlet region of the upper-0° nozzle is lower than that in the inlet region of the lower-180° nozzle.

Figure 22 shows the stress distribution of the tool at different particle sizes, derived from the ANSYS analysis. It can be seen that the stress distribution patterns are similar.

Figure 23 illustrates the variation of stress with the particle size. It can be seen that the stress decreases with increasing particle size. Coupling with the propant distribution shown in Figure 12, it can be deduced that the lower parts of the upper and lower nozzles are subjected to particle impact. As the particle size increases, the stress on the tool decreases gradually and the erosion rate also decreases.

4.2.3. Particles Mass Concentration. Given the fracturing fluid with a viscosity of 0.003 Pa·s, a flow rate of 2.1 m^3/min, a particle size of 0.4 mm, and a particle injection velocity consistent with the fluid flow velocity, a numerical simulation is conducted at the particle mass concentration of 80, 100, 120, 140, and 160 kg/m^3, respectively. Then, the erosions in the inlet

https://doi.org/10.1021/acsomega.3c09102
ACS Omega 2024, 9, 11686−11700

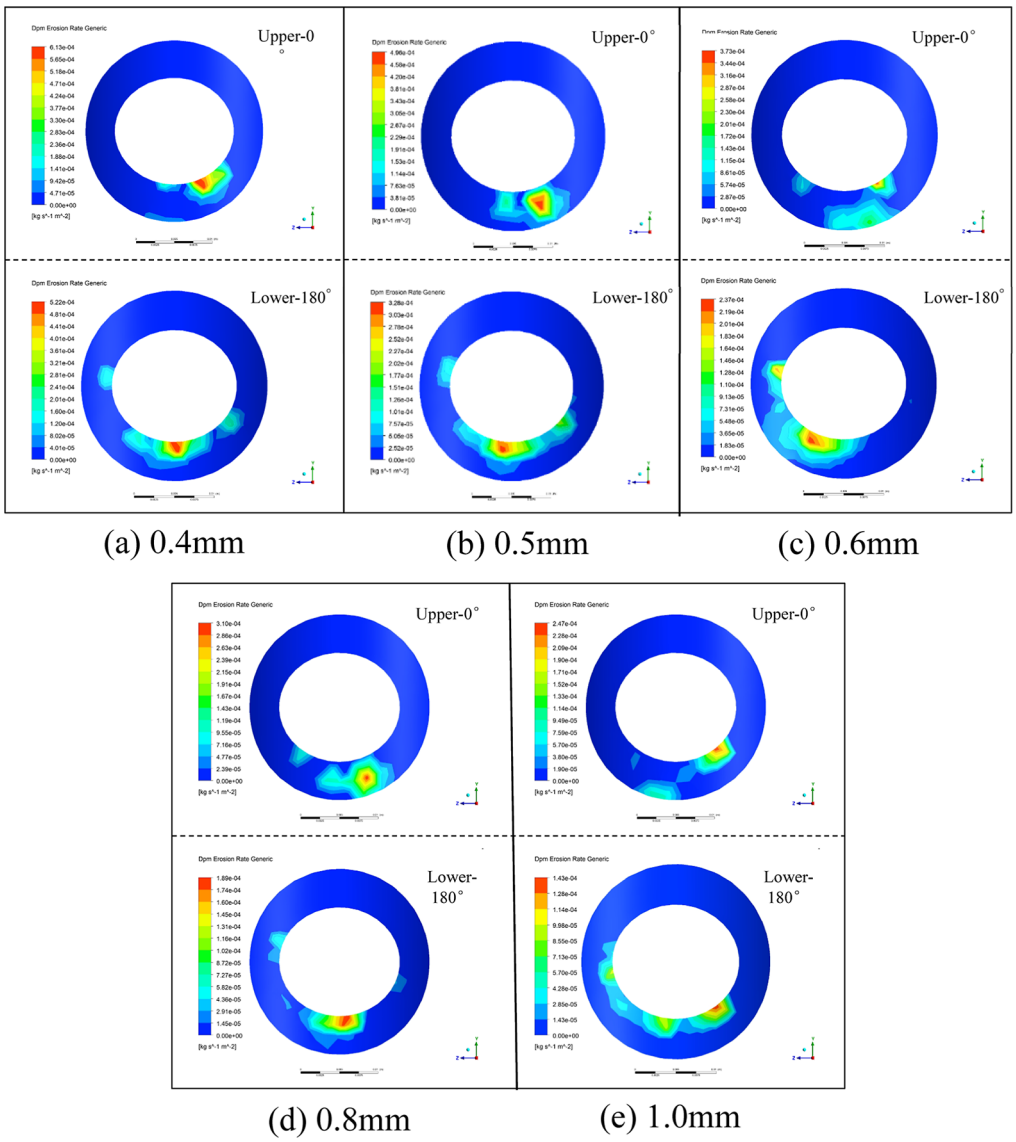

Figure 19. Erosion rate in the inlet regions of the upper-0° and lower-180° nozzles at different particle sizes.

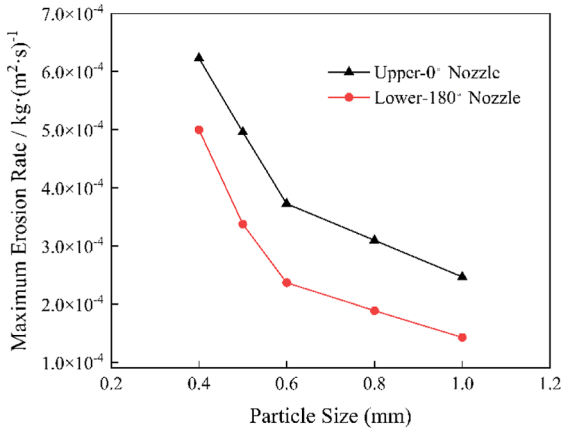

Figure 20. Maximum erosion rate vs particle size in the inlet regions of the upper-0° and lower-180° nozzles.

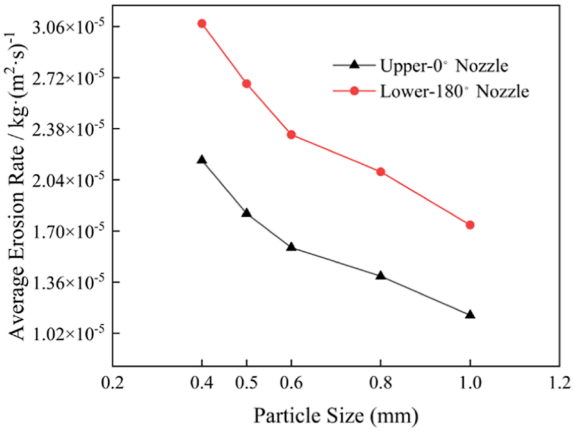

Figure 21. Average erosion rate vs particle size in the inlet regions of the upper-0° and lower-180° nozzles.

regions of the upper-0° and lower-180° nozzles at different particle mass concentrations are determined, as shown in Figure 24. It can be seen that the maximum erosion rates in the upper nozzle are concentrated in the lower right corner of the inlet region. Moreover, the lower nozzle exhibits a larger erosion area,

https://doi.org/10.1021/acsomega.3c09102
ACS Omega 2024, 9, 11686−11700

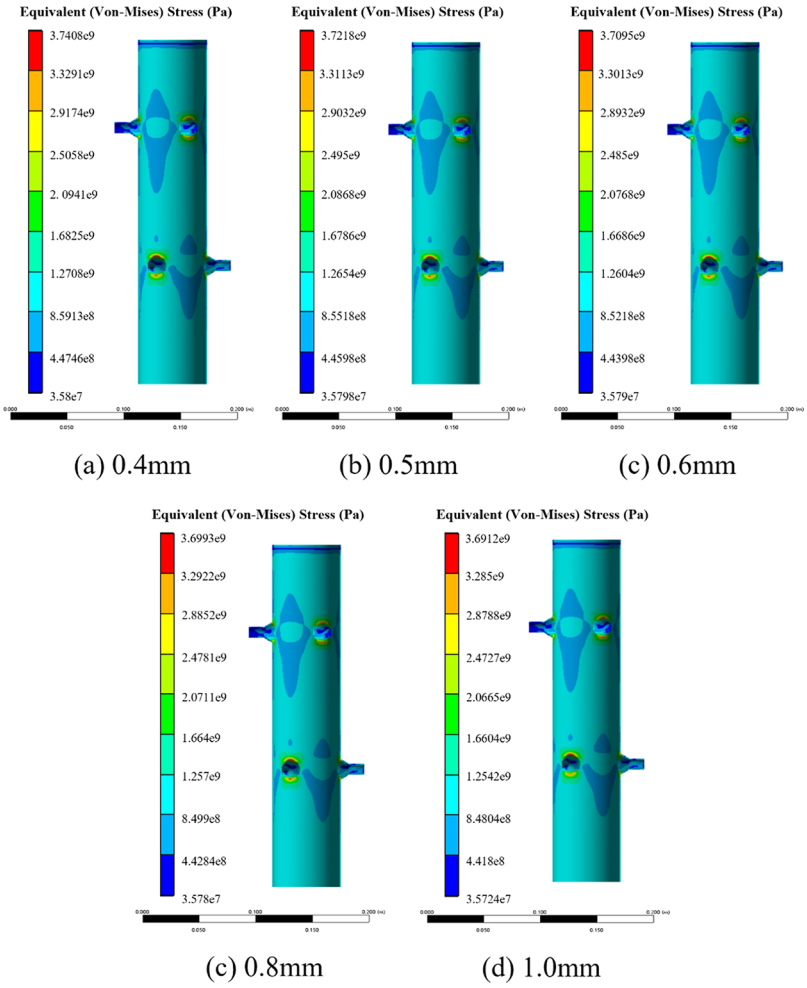

Figure 22. Stress distribution at different particle sizes.

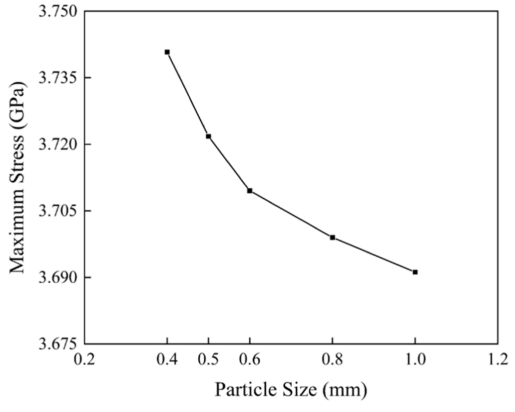

Figure 23. Maximum stress vs particle size.

with the maximum erosion rates concentrated in the lower part of the inlet region.

Figure 25 shows the maximum erosion rates at different particle mass concentrations. It can be seen that the maximum erosion rate gradually increases with the increase of the particle mass concentration. At each particle mass concentration, the maximum erosion rate in the inlet region of the upper-0° nozzle is higher than that in the inlet region of the lower-180° nozzle. With the increase of the particle mass concentration, the particle mass flow rate and the number of proppant particles increase, and there are more particles colliding with the tool body and nozzles per unit time and more particles imposing higher cutting force on the tool body and nozzles, ultimately leading to the increase of the maximum erosion rate.

Figure 26 shows the average erosion rates at different particle mass concentrations. As the particle mass concentration increases, more particles enter into the tool per unit time; thus, the average erosion rate gradually increases. At each particle mass concentration, the average erosion rate in the inlet region of the upper-0° nozzle is lower than that in the inlet region of the lower-180° nozzle.

Figure 27 shows the stress distribution of the tool at different particle mass concentrations derived from the ANSYS analysis. Similar stress concentration patterns can be observed.

Figure 28 illustrates the variation of the maximum stress with the particle mass concentration. A linear relationship is found; that is, the maximum stress increases with the increasing particle mass concentration. Coupling with the propant distribution shown in Figure 12, it can be deduced that the lower parts of the upper and lower nozzles are subjected to particle impact. As the particle mass concentration increases, the stress on the tool increases gradually and the erosion rate also increases.

5. RESULTS AND DISCUSSION

Based on the CFD and erosion theory, the erosion and stress on a small-diameter hydrajet fracturing tool under different

https://doi.org/10.1021/acsomega.3c09102
ACS Omega 2024, 9, 11686−11700

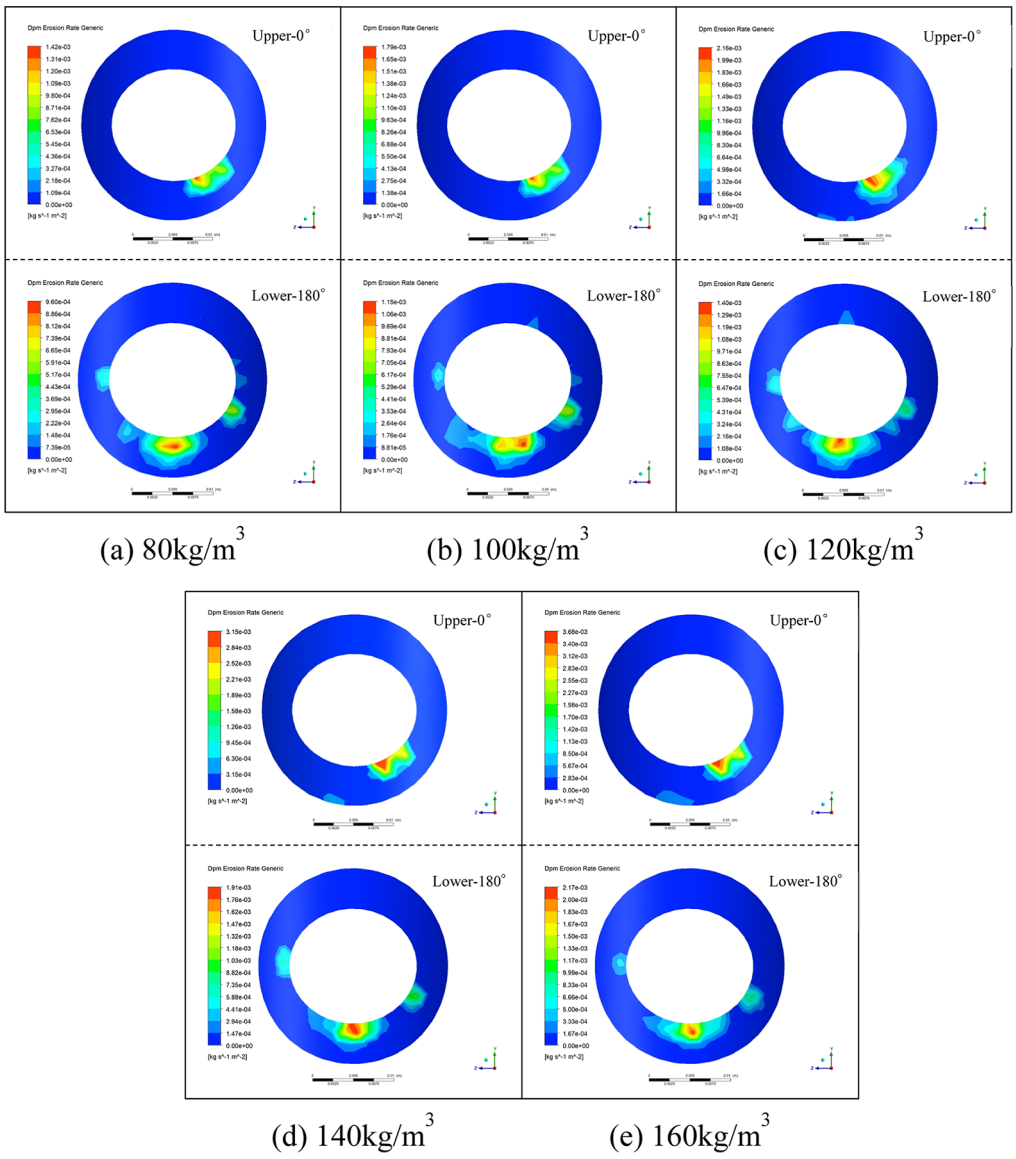

Figure 24. Erosion rate in the inlet regions of the upper-0° and lower-180° nozzles at different particle mass concentrations.

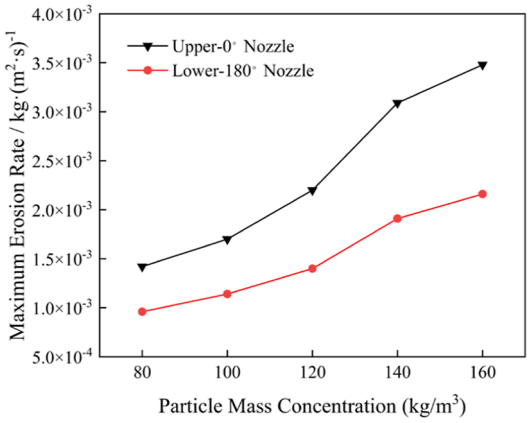

Figure 25. Maximum erosion rate vs particle mass concentration in the inlet regions of the upper-0° and lower-180° nozzles.

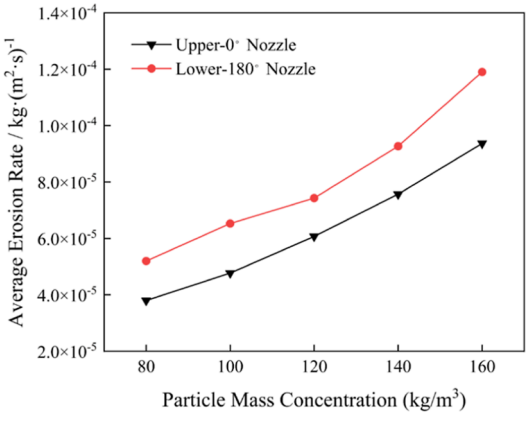

Figure 26. Average erosion rate vs particle mass concentration in the inlet regions of the upper-0° and lower-180° nozzles.

operating conditions are simulated. The following results are concluded:

1 Erosion on the internal wall of the tool body is concentrated in the inlet regions of the upper and lower nozzles, especially in the lower parts of the nozzles. Under

https://doi.org/10.1021/acsomega.3c09102
ACS Omega 2024, 9, 11686−11700

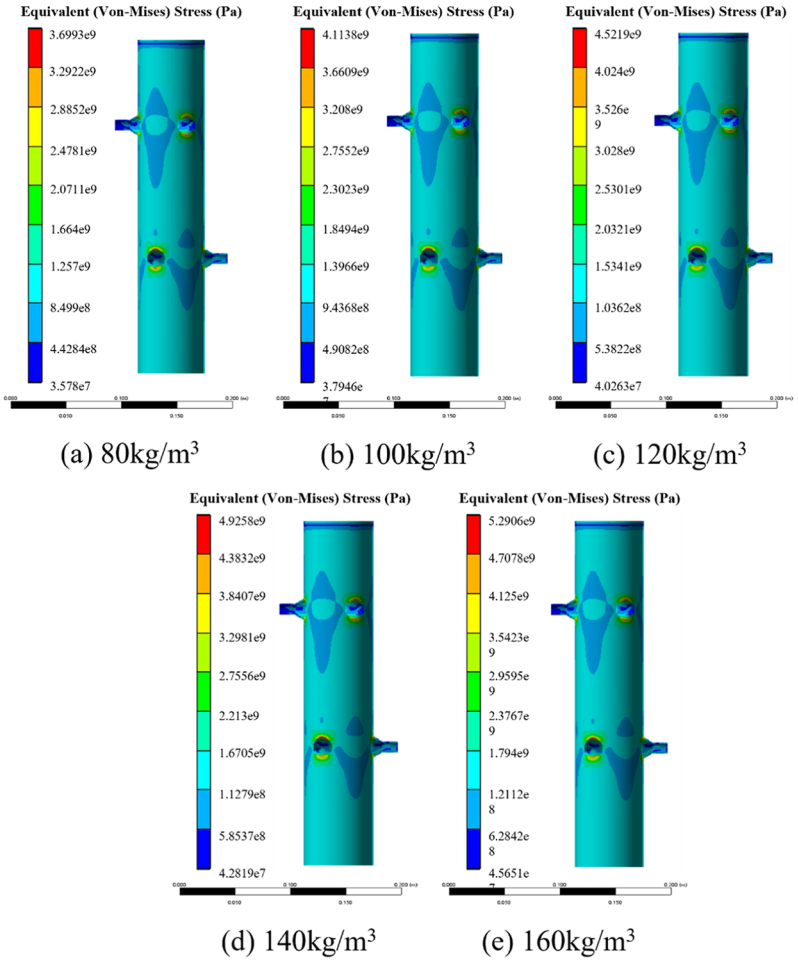

Figure 27. Stress distribution at different particle mass concentrations.

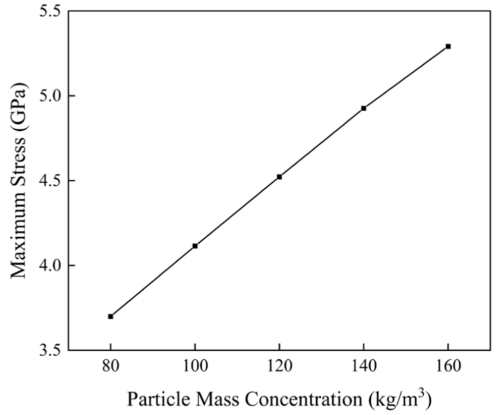

Figure 28. Maximum stress vs particle mass concentration.

each operating condition, the average erosion rate in the inlet region of the lower nozzle is higher than that in the inlet region of the upper nozzle, and the maximum erosion rate occurs in the inlet region of the upper nozzle.

2 The maximum erosion rate, average erosion rate, and maximum stress on the wall near the nozzle during fracturing increase as the inlet flow rate and particle mass concentration increase and decrease as the proppant particle size increases.

3 The erosion rate and stress of the tool are influenced by flow rate, proppant particle size, and particle mass concentration. Notably, the flow rate exhibits the most significant impact.

4 The small-diameter hydraulic fracturing tool has proven to be highly effective in enhancing and reforming oil and gas reservoirs, as well as increasing the production capacity and recovery rates of wells. This is particularly significant in the context of unconventional energy sectors, such as shale gas and natural gas development. In order to mitigate the erosion of the tool's inner wall surface, strategies such as selecting materials with superior anti-erosion properties or increasing the wall thickness can be employed to minimize wear on the tool body.

AUTHOR INFORMATION

Corresponding Authors

Jing Zhang − *Research Institute of Petroleum Exploration and Development, Beijing 100083, PetroChina*; Email: zing@petrochina.com.cn

Yiqun Zhang − *College of Safety and Ocean Engineering and State Key Laboratory of Natural Gas Hydrate, China University of Petroleum, Beijing 102249, P. R. China*; orcid.org/0000-0002-8997-667X; Email: zhangyq@cup.edu.cn

Authors

Zhenqiang Xu − *National Engineering Research Center of Gas Hydrate Exploration and Development, Guangzhou Marine Geological Survey, Guangzhou 510075 Guangdong, China*

https://doi.org/10.1021/acsomega.3c09102
ACS Omega 2024, 9, 11686−11700

Xu Cui − *College of Safety and Ocean Engineering, China University of Petroleum, Beijing 102249, P. R. China*
Kaixiang Shen − *National Engineering Research Center of Gas Hydrate Exploration and Development, Guangzhou Marine Geological Survey, Guangzhou 510075 Guangdong, China*
Xiaoya Wu − *College of Petroleum Engineering, China University of Petroleum, Beijing 102249, P. R. China*

Complete contact information is available at:
https://pubs.acs.org/10.1021/acsomega.3c09102

Notes

The authors declare no competing financial interest.

■ ACKNOWLEDGMENTS

This work was financially supported by Marine Economy Development Foundation of Guangdong Province (GDNRC[2022]44) "Technical Support for Stimulation and Testing of Gas Hydrate Reservoirs" and the National Natural Science Foundation of China (no. 52174009).

■ REFERENCES

(1) Jia, C.; Zheng, M.; Zhang, Y. Unconventional hydrocarbon resources in China and the prospect of exploration and development. *Petrol. Explor. Dev.* **2012**, *39*, 139−146.
(2) Ning, N.; Hong-yan, W.; Hong, Y.; Hong-lin, L. I. U.; Xu-jian, H. U.; Qun, Z.; De-xun, L. I. U. The unconventional natural gas resources and exploitation technologies in China. *Nat. Gas. Ind.* **2009**, *29*, 9−12.
(3) Zhang, D.; Zhang, J.; Wang, Y.; Tang, Y.; Yu, W. China's unconventional oil and gas exploration and development:progress and prospects. *Resour. Sci.* **2015**, *37*, 1068−1075. Article
(4) Hu, W.-r. Necessity and feasibility of PetroChina mature field redevelopment. *Petrol. Explor. Dev.* **2008**, *35*, 1−5.
(5) Liu, H.; Wang, F.; Wang, Y.; Gao, Y.; Cheng, J. Oil well perforation technology: Status and prospects. *Petrol. Explor. Dev.* **2014**, *41*, 798−804.
(6) Xie, Y. Exploration and practice of low permeability reservoirs exploration and development in western South China Sea. *China Offshore Oil Gas* **2018**, *30*, 80−85.
(7) Shan, L.; Zhang, W.; Luo, X. The Key Reservoir Fracturing Transformation Technology and Development Trend about the Shale Gas. *Geol. Sci. Technol. Inf.* **2013**, *32*, 156−162.
(8) Song, Y.; Zhao, S.; Wang, X.; Li, Y.; Ma, F. Friction resistance reduction technology for fracturing deep gas reservoirs. *Special Oil Gas Reservoirs* **2012**, *19*, 123−125.
(9) Zhao, J.; Wang, S.; Li, Y. Difficulties and key techniques in the fracturing treatment of shale gas reservoirs. *Nat. Gas. Ind.* **2012**, *32*, 46−49.
(10) He, X.; He, G.; Gao, Y.; Zhang, L.; He, Q.; Zhang, P.; Wang, W.; Huang, X. J. N. G. I. B. Progress in and research direction of key technologies for normal-pressure shale gas exploration and development,*Nat. Gas Ind.* 2023 *10* 555.
(11) Tang, Y.; Zhang, J.; Zhang, Q.; Long, P. An analysis of hydraulic fracturing technology in shale gas wells and its application. *Nat. Gas. Ind.* **2010**, *30*, 33−38.
(12) Jia, J.; Ge, J.; Zhen, W.; Zhao, D. Research and application of anti-reflection technology of hydraulic fracturing. *China Saf. Sci. J.* **2020**, *30*, 63−68.
(13) Zhilong, L.; Jin, Z.; Xiuxi, W.; Hengan, W. U.; Bing, X. U. E. Simulation study of characteristics of hydraulic fracturing propagation. *Rock Soil Mech.* **2009**, *30*, 169−174.
(14) Luyuan, W.; Zhenzhong, X. U.; Shiyue, C.; Shuqing, Y.; Zaitian, M. A. Identity Symbol and Prospects of Hydrate Gas. *Mar. Sci. Bull.* **2006**, *25*, 55−63.
(15) Xiaosen, L. I. Progress in researches on exploration and exploitation for natural gas hydrate. *Mod. Chem. Ind.* **2008**, *28*, 1−13.
(16) Xu, Z.; Hu, T.; Pang, X.-Q.; Wang, E.-Z.; Liu, X.-H.; Wu, Z.-Y.; Chen, D.; Li, C.-R.; Zhang, X.-W.; Wang, T. J. P. S. Research progress and challenges of natural gas hydrate resource evaluation in the South China Sea. *Petrol. Sci.* **2022**, *19*, 13−25.
(17) Zhou, H.; Peng, X.; Ye, Y. Development in technology of prospecting and exploitation for gas hydrates. *Geol. Prospect.* **2002**, *38*, 70−73.
(18) Huang, M.; Wu, L.; Ning, F.; Wang, J.; Dou, X.; Zhang, L.; Liu, T.; Jiang, G. Research progress in natural gas hydrate reservoir stimulation. *Nat. Gas. Ind.* **2022**, *42*, 160−174.
(19) Huang, H.; Yu, X.; Yu, D.; Ma, C.; Lei, P.; Tan, F.; Wang, Q. Tools for finely stratified fracturing in wells with casing deformation. *Oil Drill. Prod. Technol.* **2016**, *38*, 700−704.
(20) Wen-kui, L. I.; Jian-jun, C.; Yun, W.; Guang-hou, Z.; Yan, L. I. U.; Guang-qiang, C. A. O.; Xiang, L. I. U. The status-quo of slim hole drilling technology in China and the world. *Nat. Gas. Ind.* **2009**, *29*, 54−56.
(21) Yaoqing, A. N.; Jianguo, J. I. N.; Yuling, D.; Chuanguo, Q. I.; Bo, Z.; Shurong, Z. Study and application of fracturing techniques in slim hole and casing deformation wells. *Oil Drill. Prod. Technol.* **2009**, *31*, 119−123.
(22) Enyuan, Z.; Bairu, X. I. A.; Shiqiang, Z. H. A.; Jiaoyin, A. I. Technique of tapping the potential of residual oil in casing damage wells based on side tracking. *Oil Drill. Prod. Technol.* **2009**, *31*, 69−72.
(23) Liu, X.; Zhu, S.; Li, B.; Wang, J.; Yu, Z.; Zhang, H. Large-scale fracturing technology suitable for casing damaged wells in Daqing Oilfield and its supporting tools. *Oil Drill. Prod. Technol.* **2018**, *40*, 499−502.
(24) Jianxin, D.; Yihua, F.; Zeliang, D.; Peiwei, S. Wear behavior of ceramic nozzles in sand blasting treatments. *J. Eur. Ceram. Soc.* **2003**, *23*, 323−329.
(25) Clem, N.; Coronado, M.; Mody, R. *Utilizing Computational Fluid Dynamics (CFD) Analysis as a Design Tool in Frac-Packing Applications To Improve Erosion Life*; Society of Petroleum Engineers, 2006.
(26) Sheng, M.; Huang, Z.-W.; Tian, S.-C.; Zhang, Y.; Gao, S.-W.; Jia, Y.-P. J. P. S. CFD analysis and field observation of tool erosion caused by abrasive waterjet fracturing. *Petrol. Sci.* **2020**, *17*, 701−711.
(27) Li, J.; Hamid, S.; Oneal, D. *Prediction Of Tool Erosion In Gravel-Pack and Frac-Pack Applications Using Computational Fluid Dynamics (CFD) Simulation*; Petroleum Engineering Certification, 2005.
(28) Zhaoyang, Z. *Friction Analysis of Hydraulic Injection Fracturing of Small Diameter Oil Pipe*; Russian-korean International Symposium on Science & Technology IEEE Xplore, 2016; Vol. *30*.
(29) Xu, A.; Dou, Y.; Feng, C.; Zheng, J.; Cui, X. Coiled Tubing Erosion Prediction and Fracturing Fluid Parameters Optimization During Hydraulic Jet Fracturing. *J. Fail. Anal. Prev.* **2022**, *22*, 1276−1292.
(30) Mcdaniel, B. W.; Surjaatmadja, J. B.; East, L. E. *Hydrajet (Abrasive) Perforating Can. Improve Success of Fracturing Stimulations*; International Petroleum Technology Conference, 2008.
(31) Surjaatmadja, J. B.; Bezanson, J.; Lindsay, S. D.; Ventosilla, P. A.; Rispler, K. A. J. W. O. New Hydra-Jet Tool Demonstrates Improved Life for Perforating and Fracturing Applications. *World Oil* **2008**, *229*, 11.
(32) Cui, L.; Huang, S.; Kang, W.; Dou, Y.; Wang, Z.; Ran, Y. Study on erosion of multi-nozzle hydraulic jet tools under perforation condition. *Oil Drill. Prod. Technol.* **2018**, *40*, 620−625.
(33) Liu, H.; Mu, H. Study on erosion wear of fracturing pipe caused by solid proppant in sand fracturing. *J. Saf. Sci. Technol.* **2018**, *14*, 87−94.
(34) Zhang, Y. *Application and Improvement of Computational Fluid Dynamics (CFD) in Solid Particle Erosion Modeling*; The University of Tulsa, 2006.
(35) Iacobello, G.; Ridolfi, L.; Scarsoglio, S. J. P. A. S. M.; Applications, i. A review on turbulent and vortical flow analyses via complex networks. *Phys. A* **2021**, *563*, 125476.
(36) Wang, J.; Jiang, W.; Kong, F.; Su, X.; Chen, H. Numerical Simulation of Solid-liquid Two-phase Turbulent Flow and Wear

Characteristics of Centrifugal Pump. *Trans. Chin. Soc. Agric. Mach.* **2013**, *44*, 53−60.
(37) Wu, D.; Cai, S.; Yang, W.; Wang, W.; Wang, Z. Simulation and experiment of backfilling pipeline transportation of solid-liquid two-phase flow based on CFD. *Chin. J. Nonferrous Metals* **2012**, *22*, 2133−2140.
(38) Zhao, B.; Yuan, S.; Liu, H.; Huang, Z.; Tan, M. Simulation of solid-liquid two-phase turbulent flow in double-channel pump based on Mixture model. *Trans. Chin. Soc. Agric. Eng.* **2008**, *24*, 7−12.
(39) Veritas, N. *Recommended Practice, RP O501: Erosive Wear in Piping Systems*; Det Norske Veritas, 2007.
(40) Forder, A.; Thew, M.; Harrison, D. A numerical investigation of solid particle erosion experienced within oilfield control valves. *Wear* **1998**, *216* (2), 184−193.
(41) Peng, W. C.; Cao, X. Numerical prediction of erosion distributions and solid particle trajectories in elbows for gas−solid flow. *J. Nat. Gas Sci. Eng.* **2016**, *30*, 455−470.
(42) Zhang, Y. *Analysis on Flow Field and Wear Properties of Hydra-jet Fracturing Tool*; China University of Petroleum: Beijing, 2017.
(43) Zhaoyang, Z. *Friction Analysis of Hydraulic Injection Fracturing of Small Diameter Oil Pipe*; Xi'an Petroleum University, 2015.

https://doi.org/10.1021/acsomega.3c09102
ACS Omega 2024, 9, 11686−11700